Photothermal circular dichroism studies of single nanoparticles

Späth, P.R.

3

Photothermal circular dichroism of single nanoparticles rejecting linear dichroism by dual modulation

Circular dichroism (CD) is the property of chiral nanoobjects to absorb circularly polarized light of either handedness to different extents. Photothermal microscopy enables the detection of CD signals with high sensitivity and provides a direct absorptive response of the samples under study. To achieve CD measurements at the single-particle level one must reduce such artefacts as leakage of linear dichroism (LD) and residual intensity modulation. We have simulated our setup with a simple model, which allows us to tune modulation parameters to obtain a CD signal virtually free from artefacts. We demonstrate the sensitivity of our setup by measuring the very weak inherent CD signals of single gold nanospheres. We furthermore demonstrate that our method can be extended to obtain spectra of the full absorptive properties of single nanoparticles, including isotropic absorption, linear dichroism and circular dichroism. We then investigate nominally achiral gold nanoparticles immersed in a chiral liquid. Carefully taking into account the intrinsic chirality of the particles and its change due to heat-induced reshaping, we find that the chiral liquid carvone surrounding the particle has no measurable effect on the particles' chirality, down to g-factors of 3×10^{-4}.

This chapter is based on the publication in ACS Nano **15**, 10 (2021).

3.1. Introduction

Circular dichroism (CD) is exhibited by chiral molecules or structures that display different absorption for circular polarized light of either handedness. This absorptive property provides valuable structural information about the molecules or the objects under study. The dispersive counterpart of CD is called circular birefringence (CB) and is considered less often, although the CB and CD spectra, being related by a Kramers-Kronig relation [1, 2], have the same physical content. Several other groups have specifically designed plasmonic and dielectric structures to enhance the weak light-molecule interaction [3–9], either by enhancing the local field or by enhancing the helicity of the field. Both chirality enhancement approaches lead to an increased differential absorption (g-factor). The ultimate goal of both approaches, field or helicity enhancement, is to eventually sense chirality (CD and CB) at the single-molecule level. However, this very ambitious goal is still extremely remote. Here, we propose to improve the sensitivity of pure CD measurements of single nanoparticles in an optical microscope. CD is typically measured on large ensembles of the analytes of interest, in transmission through a solution. The light polarization is modulated at high frequencies and the polarization-dependent transmission is analyzed with a lock-in amplifier. Modern CD spectro-polarimeters operate according to a dual-polarization modulation scheme, described by Jellison et al. [10, 11]. This scheme facilitates the simultaneous measurement of multiple optical properties. This method is a standard way to obtain CD spectra of drugs and biomolecules including proteins, providing a sensitivity to differential absorptions as low as 10^{-5}. However, due to their requirement of large volumes of analyte, these spectro-polarimeters naturally lack spatial resolution and therefore are not suitable to perform CD measurements on single nanoparticles or even on minute quantities of biomolecules. In bulk measurements on solutions, the linear dichroism (LD), i.e., the differential absorption of individual molecules or particles for light polarized linearly in different directions naturally vanishes in the orientational average, unlike their CD. At the single-particle level, however, LD can be very strong, e.g., because of shape-dependent plasmon resonances. Therefore, conventional CD spectroscopy is difficult to apply to single LD-active particles or to small ensembles thereof, because of cross talk between LD and CD signals, hereafter referred to as LD-to-CD leakage.

An extinction-based approach to CD measurements of single nanoparticles was proposed by Markovich and coworkers [12]. In their scheme, the probing beam must fulfill very strict polarization requirements, not only on the excitation path but also on the detection path. A single-laser method that aims at high spatial resolution requires strongly focused light and thereby large-NA objectives. Under these tight focusing conditions, the polarization distribution in the focus plane is complex [13], due to contributions of the large span of angles necessary to produce a diffraction-limited focus. Moreover, the high NA renders the technique prone to artefacts owed to tiny imperfections of the beam alignment [14]. Any offset of the beam from the center of the objective will lead to a difference in the intensity distribution in the focus for different polarizations. This difference can easily be as large as 10^{-2} in relative intensity units, even for small beam deviations. Thus, these artefacts can easily dominate typical CD values.

Recently, we proposed a photothermal microscopic technique to image CD [15] which, thanks to its two-color scheme, separates the two conflicting requirements of polarization

purity and high spatial resolution. As the heating beam is only weakly focused, due to Koehler illumination, there are no large angles in the focus plane, which greatly facilitates high polarization purity in the focus. At the same time, the strongly focused probe beam that only senses heating effects ensures a high spatial resolution. Additionally, because it relies on the photothermal effect, the technique provides the direct absorptive response of the sample, free from scattering and birefringence contributions. Our first demonstration experiment [15], despite its high sensitivity, was prone to a number of artefacts due to the single, square-wave modulation scheme of the polarization of the heating beam. Herein, we propose a series of improvements to remedy these defects.

A first artefact that must be eliminated is residual intensity modulation of the probe or pump beam that possibly occurs at the measurement frequency of CD. We utilize a dual-modulation method similar to the one described by Jellison et al. [11] using two sinusoidally driven polarization modulators, a photo-elastic modulator (PEM) and an electro-optical modulator (EOM) and demodulate the signal at their sum frequency, here $\omega_1 + \omega_2$. The choice of at least one EOM is convenient to fulfill the requirement of a tunable bias retardation, whose importance is explained in the Supporting Information (SI). The mechanical oscillation of the piezoelectric actuators of the PEM can cause tiny vibrations at the PEM modulation frequency and lead to residual modulation of the collected probe light intensity and to a background signal. Likewise, the electro-optic modulator exhibits a slight residual intensity modulation on top of the polarization modulation, due to photoelastic scattering. This effect, also referred to as residual amplitude modulation [16, 17] leads to undesired intensity modulation of the heating beam at the driving frequency of the EOM modulator. Both the PEM's and the EOM's intensity modulations will cause artefact CD signals for any absorbing sample if CD is measured directly at the driving frequency of the individual modulators.

A second artefact that has to be taken care of is the possible cross talk between LD and CD effects [11, 18–21]. This artefact is mainly induced by static linear birefringence of the optical components, and in the special case of quarter-wave plates (QWP) by deviations from the perfect $\pi/2$ retardation. When performing measurements of ensembles of isotropically distributed molecules or particles in solution, linear dichroic effects can be neglected thanks to ensemble averaging. When performing CD studies of individual plasmonic particles, it is crucial to avoid this cross talk as the LD of plasmonic particles can easily exceed their CD by some orders of magnitude. Any sample exhibiting LD can cause an artefact signal in a CD measurement. When LD-to-CD leakage is not carefully removed, it can lead to erroneous interpretations of the results. The reverse effect, CD-to-LD leakage, although present in principle, can be neglected as long as CD is much weaker than LD.

To solve all problems of residual intensity modulation and of the cross-talk between CD and LD, we apply a purely sinusoidal modulation scheme based on the design of Jellison et al. [11]. We insert an additional quarter-wave plate (QWP) on the heating beam path. This QWP shifts the CD signal to the sum $\omega_2 + \omega_1$ and the difference $\omega_2 - \omega_1$ frequencies of the two modulators. We perform lock-in detection at one of these two frequencies. We have chosen the sum frequency, because we expect less 1/f noise at higher frequencies. More importantly, at these combination frequencies the small residual intensity modulations of the two modulators become second-order effects which can be safely neglected. Furthermore, if we choose the first modulator to be the EOM, we find that the cross talk of LD into CD

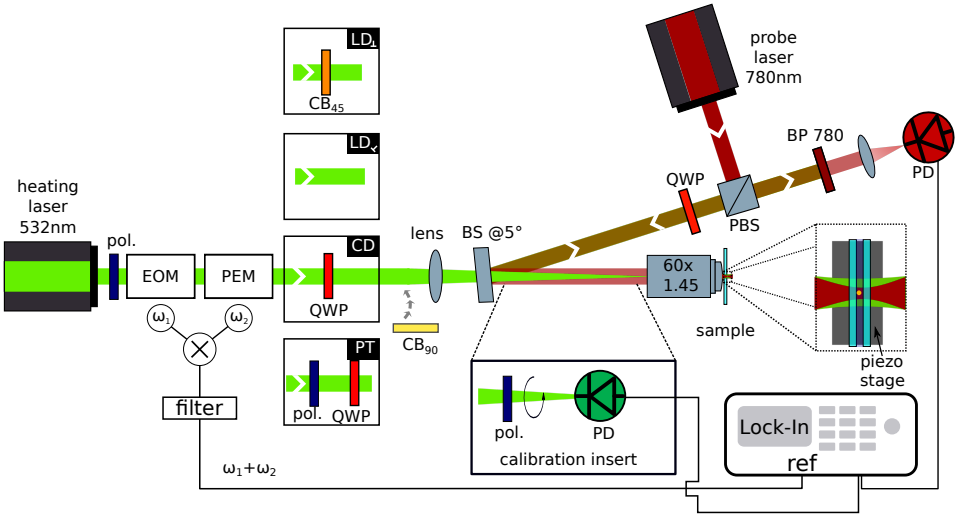

Figure 3.1: Schematic representation of the dual modulation PTCD setup with the additional calibration insert, where a rotatable calibration polarizer and photodiode (PD) can be inserted into the heating beam path. By flipping a set of different polarization components, i.e. circular birefringence plates and polarizer, we are able to measure all absorptive properties CD, $\mathrm{LD}_{\perp}$, $\mathrm{LD}_{\swarrow}$, as well as the isotropic absorption of the sample. The $532\,\mathrm{nm}$ heating laser is passed through a polarizer and two polarization modulators, the electro-optic modulator (EOM) and the photoelastic modulator (PEM). To measure PT, CD and both LDs, we insert different sets of polarization components (polarizer, quarter-wave plate (QWP) and circular birefringent plate CB_{45} which rotates the linear polarization by $45°$). The circular birefringent plate CB_{90} which rotates any linear polarization by $90°$ is used to check the leakage of LD into CD. The heating laser is focused at the back focal plane of the objective by means of a wide-field lens (focal length $50\,\mathrm{cm}$) in a Koehler scheme, to illuminate a sample area of about $20\,\mu\mathrm{m}^2$. The $780\,\mathrm{nm}$ CW probe laser is used in a configuration combining a polarizing beam-splitter (PBS) and a QWP. The probe laser is reflected at a 50/50 beam-splitter (BS) at an angle of $5°$ and focused in the sample plane using a high-NA oil-immersion objective (60X, NA=1.45). The sample is scanned using a piezo stage. The reflected probe beam at the glass-oil interface interferes with the probe beam scattered by the thermal lens. The interference signal is filtered from the heating laser using a band-pass filter (BP 780) and focused onto a photodiode connected with a lock-in amplifier. A frequency mixer is used to mix two frequencies used for modulation of the two modulators and sent to the lock-in as a reference frequency.

induced by imperfections of the optical components, such as residual static birefringence exhibited by EOM, PEM or QWP, can be compensated in a straightforward manner by combining a slight rotation of the QWP with tuning of the bias voltage of the EOM. Figure 3.1 illustrates our imaging photothermal microscope with dual polarization modulation. The setup is not only capable of measuring circular dichroism but furthermore has the capability to measure linear dichroism and the full absorption of one of the circular polarizations. Together with CD, this measurement provides the isotropic absorption that could be measured in an unpolarized photothermal experiment. It is important to stress here that, to fully retrieve the LD information, at least two measurements have to be performed, one in the [0°; 90°] basis and one in the [+45°;-45°] basis. We abbreviate the former with $\mathrm{LD}_{\perp}$ and the latter with $\mathrm{LD}_{\swarrow}$. The heating beam ($532\,\mathrm{nm}$) is polarization-modulated by the EOM and the PEM in series. It then passes a variable set of polarization optics that define the

operation mode of the setup: i) $LD_{\diagup}$ -sensitive without any additional polarization element, ii) $LD_{\perp}$-sensitive with a 45°-circular birefringent plate (or 45°-polarization rotator), iii) CD-sensitive with QWP alone, iv) photothermal absorption-sensitive (PT) with a linear polarizer (0°) and QWP. The QWP placed after the polarizer practically provides the isotropic absorption signal in the usual case of particles with very weak CD. Illumination with this intensity-modulated, circularly-polarized heating beam provides us with a signal which is very close to the regular photothermal signal, and therefore allows us to normalize the CD and LD signals to the isotropic absorption of the particle. In this manner, we calculate the g-factor of a sample by simply dividing the CD or LD measurement with the respective PT measurement

$$g_{CD(LD)} = \frac{CD(LD)}{PT}. \tag{3.1}$$

The respective FFT spectra of signals in the different measurement modes are shown in figures S3.2-S3.4. For objects with strong LD signals, a 90°-circular birefringent plate can be added [22], to further improve the cancellation of LD-to-CD leakage and other LD-related artefacts. The heating beam is weakly focused on the sample ($5\,\mu\mathrm{m}$ in the focal plane, corresponding to an effective NA of ∼0.07), whereas the probe beam (at $780\,\mathrm{nm}$) is tightly focused to retain a high spatial resolution. The reflected probe beam is then cleaned up by removing any residual heating light by means of a long-pass filter and sent to a photodiode for detection. A more detailed description of the setup and the purpose of the 90°-circular birefringent plate can be found in the SI.

3.2. Results and discussion

3.2.1. Simulations

To optimize its performance, we modeled our setup by means of Jones matrix calculus and performed simulations to choose the optimal modulation parameters and to estimate the setup's sensitivity to misalignment and imperfections of its optical components. We want to point out here that there is no need to perform a full Mueller matrix analysis as the weakly focused heating beam (∼$5\,\mu\mathrm{m}$) is free from the various depolarizing effects that can occur in tightly focused beams and in transmission methods [20]. In an ideal setup, i.e. if we were only sensitive to CD, we expect zero modulation depth at the sum (or difference) frequency when looking at purely linear dichroic samples. Due to imperfections of the optical elements, however, we have to anticipate cross talk between CD and LD. To quantify this cross talk, we calculate the rejection ratio $R_{ext} =\mid LD(\omega_1+\omega_2) \mid / \mid CD(\omega_1+\omega_2) \mid$ that we define as the ratio of the absolute value of the LD, divided by the absolute value of the spurious CD signal measured in the CD channel for a nanoparticle with pure LD absorption, without any intrinsic CD. We calculate that ratio at the sum frequency of the two modulators and under the assumption that the absorption asymmetry (g-factor) is the same for 3 ideal samples showing pure $LD_{\perp}$, $LD_{\diagup}$, and CD. Unlike other dual modulation approaches [11, 23] we keep the amplitudes of the phase modulation of the two modulators fixed (both $\pi/2$) and explore the effect of changing the EOM bias retardation and the QWP's fast axis orientation on the rejection ratio of $LD_{\perp}$ and $LD_{\diagup}$. Our goal is to find a set of modulation parameters that optimizes this rejection ratio and thereby reduces the cross talk between

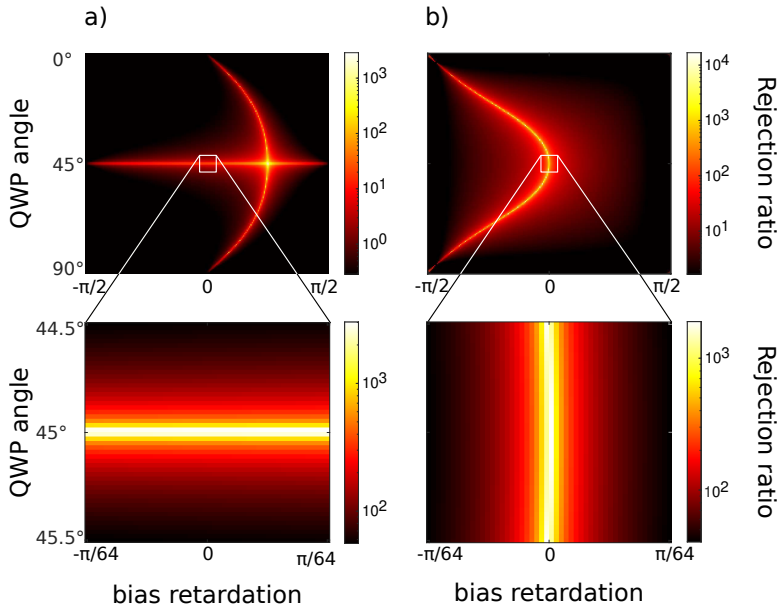

Figure 3.2: Calculated rejection ratio of (a) $LD_{\perp}$ and (b) $LD_{\swarrow}$ as a function of EOM bias retardation and QWP orientation. The zoom-in in the lower panel shows that in the region where $LD_{\perp}$ and $LD_{\swarrow}$ are both large, the rejection ratio is only dependent on one parameter, either bias voltage for $LD_{\perp}$ or QWP orientation for $LD_{\swarrow}$.

$LD_{\perp}$ or $LD_{\swarrow}$ and CD. In our model we take into account imperfections of all retarding elements, including the QWP and the bias and amplitude of retardation by the PEM and the EOM. The detailed mathematical representation is discussed in the SI.

Figure 3.2 shows a map of the calculated rejection ratio in our dual-modulation configuration as a function of EOM bias retardation (static linear birefringence) and QWP's orientation. Large rejection ratios for both $LD_{\perp}$ and $LD_{\swarrow}$ are important, especially when measuring anisotropic plasmonic particles, e.g. quasi-spherical nanoparticles (NPs) and nanorods (NRs), that can exhibit linear dichroism which is up to two orders of magnitude stronger than their circular dichroism. The lower left panel of figure 3.2 shows that the $LD_{\perp}$ rejection ratio is strongly dependent on the QWP rotation but nearly independent of the bias retardation while the lower right panel shows that $LD_{\swarrow}$ is almost independent of the QWP rotation but strongly dependent on the bias retardation. This result indicates that bias retardation and QWP rotation can be used to tune the rejection ratio of $LD_{\perp}$ and $LD_{\swarrow}$ independently.

3.2.2. Experimental results

The experimental calibration scheme of the rejection ratio is illustrated in figure 3.1. By inserting the calibration insert we can quantify and tune the setup's experimental rejection ratio of LD as described in the SI (figure S3.1). Using the calibration insert we find that our setup has a LD rejection ratio of at least 200 at all angles of the polarizer, which for

most samples we work with is a good enough value to exclude any artefacts induced by LD. It means that if the object we want to study exhibits LD that is 200 times stronger than its CD, then the artefact signal generated by the cross talk would be as large as the intrinsic CD signal. Our calibration experiments yielded a rejection ratio roughly one order of magnitude worse than the rejection ratios we find in our simulations ($\sim 10^3$). We attribute this discrepancy to the finite beam aperture of the heating laser beam and the thereby resulting spatially inhomogeneous phase retardation of the heating beam in the EOM. In later PT measurements with Koehler illumination, however, as we only use the center of the heating beam to excite the small nanoparticle, the real rejection ratio is expected to be be significantly better than the rejection ratio found upon calibration.

Aluminium nanorods

To demonstrate the strength of our technique, especially regarding the distinction between CD and LD, we have performed measurements on a purpose-tailored sample. The sample consists of nano-fabricated aluminium nanorods, designed such that they absorb the $532\,\mathrm{nm}$ pump laser strongly along their long axis, but weakly along the short axis [24], thereby exhibiting a strong LD. Aluminium NRs have higher LD g-factors than gold ones at our heating wavelength of $532\,\mathrm{nm}$ because the UV interband transitions of aluminium do not damp the visible plasmon resonance, in contrast to the case of gold [25]. The rods are immersed in toluene to provide high PT contrast. The measurement results are shown in

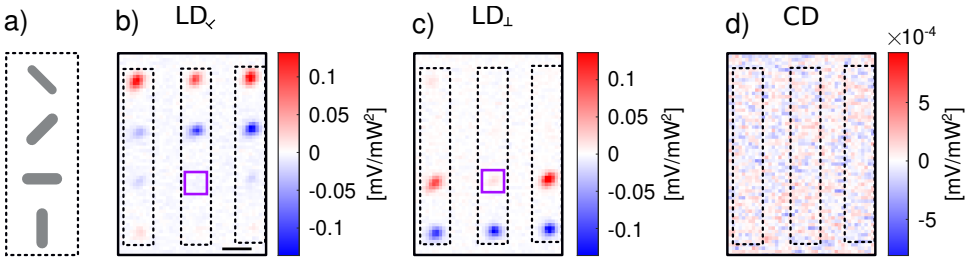

Figure 3.3: LD and CD scans of 12 aluminium NRs (size $100\times40\,\mathrm{nm}^2$, thickness $60\,\mathrm{nm}$) exhibiting strong linear dichroism. (a) illustrates the spatial orientation of the rods. (b-d) show $\mathrm{LD}_{\swarrow}$, $\mathrm{LD}_{\perp}$ and CD scans, respectively. The phase-sensitive detection enables the determination of the NRs absolute orientation via the amplitudes' sign. The absence of any observable signal in the CD measurement (d) proves the strong rejection of LD signals. The weaker residual signals in the $\mathrm{LD}_{\swarrow}$ and $\mathrm{LD}_{\perp}$ scans are due to a slight misalignment of the sample with respect to the polarization modulator axes. The square box indicates a nanorod with a reduced absorption due to a fabrication fault. The scale bar is $2\,\mu\mathrm{m}$. The probe beam intensity was $2\,\mathrm{mW}$ and the heating beam intensity was $11\,\mathrm{mW}$, measured at the entrance of the objective.

figure 3.3. We find that the NRs exhibit the expected large $\mathrm{LD}_{\perp}$ and $\mathrm{LD}_{\swarrow}$ amplitudes and that the CD signal amplitude, if there is any, is buried below the noise. This result proves that our method can discriminate the effect of CD and LD with virtually no cross talk and thereby facilitates the artefact-free measurement of samples with very weak CD. We find a rejection ratio of 313 ±9 for $\mathrm{LD}_{\perp}$ and 340 ±11 for $\mathrm{LD}_{\swarrow}$, respectively. As mentioned above, these values are significantly higher than the one found upon calibration (200), and are consistent with our calibration measurement using the entire beam aperture, whereas the nanoparticle measurement only makes use of the very center of the beam, with presumably smaller polarization imperfections. Here we assume that the NRs are perfectly achiral ob-

jects. Although this assumption holds true for ideal nanorods, fabrication errors could give rise to residual CD. In our CD measurements we do not find any measurable CD signal. Based on the SNR we can therefore give an upper bound of 3×10^{-3} for the g-factor of these rods.

CD and LD measurements at three different wavelengths

So far we have shown CD measurements only at a single wavelength. To retrieve useful structural information of a sample of interest one should record its full CD spectrum. As we had no access to a tunable heating laser with the required power, we instead used three lasers at different wavelengths, 450 nm, 532 nm and 660 nm, to show that our technique is compatible with spectral measurements. Although the EOM's retardance is strongly dependent on the beam parameters (width and pointing angles), we found our alignment method robust enough to overlap the different laser beams by means of flippable mirrors, while still keeping excellent rejection ratios. Figure 3.4 shows measurements of 100-nm-diameter quasi-spherical gold nanoparticles at three different wavelengths. For each wavelength we performed a full analysis of the absorption of the nanoparticles including isotropic absorption, linear dichroism and circular dichroism. The scans shown in figure 3.4 contain measurements of two single particles and one small cluster of particles. At a heating beam

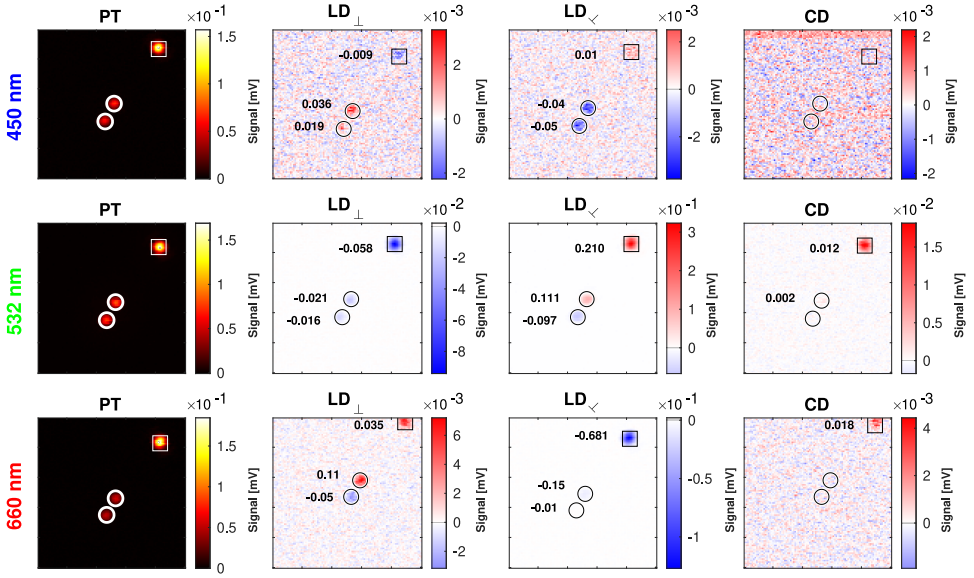

Figure 3.4: Photothermal (isotropic absorption), $LD_{\perp}$, $LD_{\swarrow}$ and CD measurements of spherical gold nanoparticles at three different wavelengths (450 nm, 532 nm, 660 nm) of the heating beam. The numbers indicated in $LD_{\perp}$, $LD_{\swarrow}$ and CD images are the averaged g-factors for each spot. A histogram of CD values for several particles is displayed in figure S3.6. The brightest particle in the PT image (square box in the upper right corner) is a dimer or trimer of nanoparticles (see figure S3.5 for more CD and LD measurements on such a dimer). The probe beam intensity was 6 mW throughout the entire experiment. The respective heating powers were 0.6 mW at 450 nm, 5 mW at 532 nm and 8 mW at 660 nm, measured at the entrance of the objective.

wavelength of 450 nm we find the particles to have both weak linear dichroism and weak

circular dichroism. This observation fits with our expectation that the interband transitions of gold strongly damp plasmonic behaviour at that wavelength, and therefore that polarization dependence is weak at this wavelength. We find relatively strong linear dichroism for both $532\,\mathrm{nm}$ and $660\,\mathrm{nm}$ heating wavelengths. This residual LD can be explained by small protrusions of the particle along one or more axes that may have formed during synthesis. Depending on the axis along which the particle is excited, one observes a different plasmon resonance wavelength and therefore linear dichroism. Notably, the particle with the strongest PT signal most likely corresponds to a dimer or trimer of nanoparticles. This cluster has a much stronger g-factor in LD than the single particles. If two nanoparticles are very close together they couple plasmonically and the degeneracy of the plasmons of the two nanoparticles may be lifted to yield two longitudinal modes, a symmetric and an antisymmetric mode, whereas the transverse plasmon resonances are not much affected. The symmetric longitudinal mode can be considerably red-shifted from the transverse mode [26]. This plasmon coupling can lead to the relatively strong LD in our measurements at both wavelengths.

The images of the single particles are barely visible in the CD scans, but the cluster shows a clear CD signal, which probably also arises from plasmonic coupling [27, 28]. The limited power of the $450\,\mathrm{nm}$ and the $660\,\mathrm{nm}$ lasers in these measurements prevented us from measuring g-factors smaller than 10^{-3}. From the strength of the PT signal at $450\,\mathrm{nm}$ and from the low CD value, we hypothesize that the cluster is composed of two or three particles. These results prove that our technique can in principle be extended to obtain the spectral dependence of CD, provided one has access to a tunable laser with sufficient power ($\sim 10\,\mathrm{mW}$ in the sample plane). The main factor that could hamper compatibility with spectral measurements in our technique is the wavelength dependence of the retarding elements. By using Koehler illumination for the heating beam we are relatively insensitive to chromatic aberrations of the lenses. However, to ensure good cancellation of cross talk between LD and CD, it is of utmost importance to ensure the correct retardance of the polarization optics. Both the EOM's and the PEM's retardance can be adjusted easily to deliver the required maximum modulation phase of $\pi/2$ for each wavelength. The QWP in use, although it is a superachromatic one, exhibits a slight dependence of its retardance on wavelength. One solution would be to compensate the wavelength dependence by making use of a liquid crystal retarder with adjustable retardance. We found that, by combining the aforementioned slight rotation of the QWP with an adjustment of the EOM bias retardation, it is possible to use a superachromatic or simply achromatic waveplate while achieving similar rejection of LD-to-CD cross talk.

Thanks to its good sensitivity and to its compatibility with spectral measurements, we foresee a great potential of our technique in the study of single plasmonic particles, including those having CD and LD bands in the near-IR range. A super-continuum laser or a Ti:Sapphire laser could conveniently provide a large spectral range while still delivering enough heating power for measuring CD g-factors down to the few 10^{-4} level. Heating in the near-IR would best be combined with a probe at even more red-shifted wavelength. We think that the technique is compatible with a transmission geometry [29, 30], which would allow one to probe in the mid-IR. In that case one can use near-IR optimized refractive objective for heating and a reflective objective for the probing. Compared to more conventional techniques based on scattering or extinction, our absorption-based detection can measure CD signals of single nanoparticles with excellent signal-to-noise ratio [5, 12, 31].

Gold nanoparticles immersed in a chiral liquid

We have characterized our setup's performance in terms of rejection of unwanted effects such as the leakage of linear dichroism or residual intensity modulation of the polarization modulators. These steps were necessary to make sure that we have the sensitivity to measure CD g-factors of single nanoparticles in the few 10^{-4} range, while at the same time avoiding cross talk induced by LD. In the experiments reported below, we wanted to investigate the very small circular dichroism of nominally achiral nanoparticles induced by a chiral liquid surrounding the particle [32]. The effect, referred to as PCCD (plasmon-coupled circular dichroism), may facilitate the detection of chirality of biomolecules in the visible, where most biomolecules have no absorption band [8]. According to the theoretical model presented in references [32, 33] PCCD has two components, one due to enhanced absorption of the molecule in the near field of the plasmonic particle, and the second one due to chiral currents induced in the nanoparticle by the molecular dipole. In the present case, the chiral liquid does not absorb in the visible, and only the latter component is left, which corresponds to heat dissipation by the particle (at the plasmon resonance, the particle's absorption dominates molecular absorption anyway).

In their more recent work, Yoo et al. [34] presented a solution of Maxwell's equations in circular bases, dubbed chiral Mie theory. They concluded that spherical gold nanoparticles, when immersed in a pure chiral liquid, can exhibit a measurable circular dichroism in the region of the particles' plasmon resonances. So far, none of the available experimental methods has been sensitive enough to detect the small PCCD signal of a single nanoparticle. Although Zhang et al. [5] have demonstrated CD measurements on single clusters of nanorods, the sensitivity limit of their technique could not resolve CD g-factors far below 10^{-1}. The sensitivity of photothermal CD, however, reaches down to g-factors of a few 10^{-4}, and might enable us to probe the magnitude of PCCD. To investigate the system proposed by Yoo et al., we spin-coated $100\,\mathrm{nm}$ spherical gold nanoparticles on a glass surface, and glued this sample onto a half-open channel to form a flow cell. We then performed measurements on the same single nanoparticles with two different liquids as photothermal media. These liquids were the pure enantiomers of carvone (pure S-carvone and pure R-carvone). For each liquid we performed isotropic absorption measurements.

Figure 3.5 shows absorption (a) and circular dichroism scans (b) of the same single nanoparticle surrounded by the pure enantiomers of opposite handedness and in (c) the corresponding calculated CD g-factors of each measurement. The measurements were carried out with a heating wavelength of $532\,\mathrm{nm}$. We find that the particle initially exhibits weak CD (see figure 3.5(c)) when immersed in S-carvone. To find out whether this initial CD is due to geometric distortions of the particle itself or due to CD induced by the chiral liquid (PCCD) we flush the sample cell with R-carvone which is of opposite handedness and perform another set of absorption measurements. The PT signal, which represents the isotropic absorption of the particle, remains practically unchanged (3.5(a) S1 and R1). If the initial CD signal was due to the chiral liquid then its sign should change upon reversal of the liquid's handedness. We find, however, (3.5(c)), that the change of CD is negligible within noise. That means that the measured CD is due to geometric chirality of the particle itself and, more importantly, that the chiral liquid does not alter the particle's CD by more than a g-factor of 3×10^{-4}. Repeating the experiment by measuring in both liquids again (measurements S2 and R2) reproduces our findings that the changes of CD signals are within noise.

We confirm the absence of residual leakage of LD into CD by performing LD reference measurements which are shown in figure S3.6. The residual leak of LD, considering our rejection ratio of 300 is one magnitude smaller than the measured CD signal and can therefore be safely neglected. We want to note here that the sensitivity of the measurements was limited due to heating-induced reshaping of the particles [35–37]. In order to avoid reshaping, we had to use heating powers below $20\,\mathrm{mW}$. Higher powers cause long term changes of the PT signal as shown in figure S3.7. The results of Yoo et al. [34] predict a differential

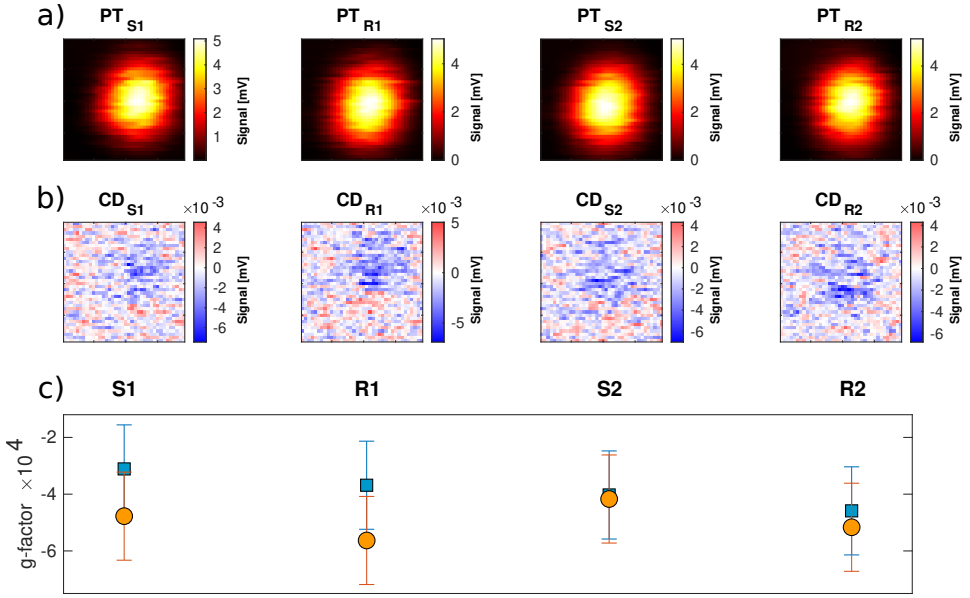

Figure 3.5: Photothermal (a) and photothermal circular dichroism (b) measurement of a single $100\,\mathrm{nm}$ diameter spherical gold nanoparticle immersed in the two pure enantiomers of the carvone molecule (S carvone and R carvone). (c) shows the corresponding g-factors of the scans. We employed two methods to calculate the g-factor. For the blue data points we use all pixels of the scan, for the orange data points we use a 20×20 pixel array around the centroid position of the corresponding PT scan. The heating beam intensity was $17\,\mathrm{mW}$ and the probe beam intensity was $2.5\,\mathrm{mW}$

absorption of about 10^{-2} for a liquid with a large circular birefringence (CB) of 10^{-2}. The circular birefringence of carvone corresponds to a difference in refractive indices for circular polarization of about 10^{-4} [38, 39]. Scaling the results of Yoo et al. linearly with CB, we therefore expect an induced CD of about 10^{-4} in carvone, in good agreement with the estimations of reference [33]. This value is below, or close to our detection limit. Therefore, despite our improved sensitivity, we are not able to report any measurable PCCD effect for a gold nanoparticle in carvone heated with $532\,\mathrm{nm}$. Reshaping of the particle, laser-induced chemical reactions [40] and instabilities or drifts of our optical setup set a limit to our detection sensitivity of PCCD (see SI, Sec. "Heat-induced reshaping"). To improve on this result, one could consider using other shapes of plasmonic particles, such as nanorods or nanocubes, which present a stronger dependence of absorption on the surrounding refractive index due to their sharper plasmon resonances. These particles, however, are even more

prone to reshaping than quasi-spherical particles [35]. The lower powers needed to avoid reshaping would lower the photothermal sensitivity. Another strategy would be to enhance PCCD by choosing a surrounding medium with a larger circular birefringence. Alternatively, we might be able to improve the measurement sensitivity further by employing more efficient contrast mechanisms, as recently demonstrated in refserences [41–43]. This would allow us to observe g-factors down to the 10^{-4} range while at the same time substantially decreasing the heating and therefore avoiding reshaping.

3.3. Conclusion

We have improved our previously reported PTCD microscope [15] by the addition of dual modulation of the polarization and of a QWP. We achieved CD measurements with excellent rejection of artefacts induced by vibrations, residual amplitude modulation, residual linear birefringence, and we removed leakage of linear dichroism into circular dichroism down to below our detection limit. Compared to our previous single square-wave modulation scheme [15], we suppressed these artefacts by nearly two orders of magnitude. Additionally, by means of a set of static birefringent elements, we can retrieve the full polarization dependence of a single particle's absorption. Our simulations provide a simple tool to understand how to optimize modulation parameters to avoid, or to compensate for, residual depolarizing effects of the optics. We have experimentally demonstrated the rejection of LD leakage into CD by more than a factor of 200 allowing us to measure weak CD signals of single quasi-spherical gold nanoparticles with a high sensitivity down to 3×10^{-4} in g-factors. Furthermore, we also show the capability of the method to perform spectral CD measurements. Studying nominally achiral plasmonic nanoparticles in a chiral liquid environment, we could not detect any significant plasmon-induced transfer of chirality from the liquid to the particle. We therefore find a PCCD upper bound of a 3×10^{-4} for our sample at $532\,\mathrm{nm}$. This g-factor sensitivity applies to $100\,\mathrm{nm}$ gold particles. We can translate it into a difference of absorption cross section of $\sim 6\,\mathrm{nm}^2$, independent of particle size at a fixed heating power. Smaller gold particles, however, would allow higher heating intensities, giving rise to higher sensitivities. Plasmonic systems like single particles with more complex shapes or dimers of nanoparticles may turn out to be better candidates to investigate the weak PCCD effects.

3.4. Methods and experimental

3.4.1. Experimental setup

A schematic of the experimental setup is shown in Figure S3.1. More details about the setup can be found in chapter 2. In comparison to our previous setup (which contained a single modulator, electro-optic modulator (EOM)), a second polarization modulator (photo-elastic modulator (PEM)) was added to perform dual modulation of the polarization. The EOM and PEM were sinusoidally driven at modulation frequencies 23.5 kHz and 50 kHz, respectively. In addition we have used two circular birefringent plates, CB_{90} and CB_{45} which rotate the linear polarization by $90°$ and $45°$, respectively. The heating beam diameter was $\sim 1\,\mathrm{mm}$, when propagating through the polarization modulators

3.4.2. Data analysis

g-factors for each single gold nanopshere in figure 3.4 were calculated as ratios of mean values of photothermal and photothermal circular and linear dichroism signals averaged in an area of 7×7 pixels^2 around the centroid of each spot. g-factors for the gold nanosphere in figure 3.5 were caclulated in an area of 20×20 and 38×38 pixels^2 around the centroid position, respectively. The rejection ratio of the aluminium nanorod measurements was calculated taking the mean value of a 5×5 pixel area centered around the maximum values of the respective $LD_{\perp}$ and $LD_{\swarrow}$ measurements and dividing it by the noise standard deviation of the same region in the CD image.

3.5. Supplementary information

3.5.1. Stokes representation of polarization

The Stokes parameters of polarized light are usually employed when describing partially polarized light and thus allow for a more general treatment than the Jones calculus representation of polarization. Here, even though we only deal with fully polarized light, we still introduce the Stokes definition of polarization as it provides a convenient expression of polarization states in terms of the four Stokes parameters, which are defined as

$$S_0 = \langle E_x^2 + E_y^2 \rangle$$
$$S_1 = \langle E_x^2 - E_y^2 \rangle / S_0$$
$$S_2 = \langle E_x E_y cos(\delta) \rangle / S_0$$
$$S_3 = \langle E_x E_y sin(\delta) \rangle / S_0$$

E_x and E_y are the respective *x* and *y* components of the electric field and δ is the phase difference of the two components. With this definition we have

- horizontal polarization if S_1 = 1
- vertical polarization if S_1 = -1
- linear 45° polarization if S_2 = 1
- linear -45° polarization if S_2 = -1
- right circular polarization if S_3 =1
- left circular polarization if S_3 = -1

3.5.2. Experimental alignment procedure

In this section we will give a description of the alignment procedure of the heating arm of our dual-modulation setup. The heating part of the setup, the one that is polarization-modulated, is illustrated in figure S3.1. It consists of two polarization modulators, an EOM and a PEM. A set of static birefringent elements, QWP, CB_{45} and CB_{90} changes the measurement mode

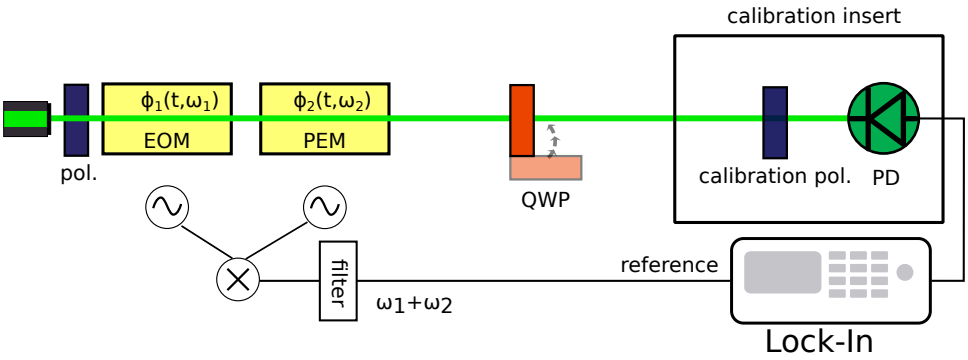

Figure S3.1: Heating arm of the dual modulation setup. The polarization modulation is performed by an EOM and a PEM, followed by a set of static retarders (QWP, CB_{45} and CB_{90}). A calibration unit composed of a rotatable polarizer and a fast photodiode is inserted for alignment of the polarization modulation. The configuration illustrated here, with the QWP inserted, corresponds to the mode sensitive to circular dichroism (CD-sensitive).

of the setup and allows us to measure different absorptive properties as explained in section 3.1. After the birefringent plates we add a calibration unit consisting of a rotatable polarizer and a fast photodiode. The photodiode's output is sent to a lock-in amplifier which is referenced to the sum frequency of the two modulators.

The purpose of the alignment procedure is to make the setup sensitive to one of the following absorptive properties, isotropic absorption, linear dichroism (LD), and circular dichroism (CD), while as much as possible reducing cross-talk between these properties. Plasmonic nanoparticles can in principle exhibit both linear dichroic and circular dichroic behaviour. In samples consisting of plasmonic nanoparticles, the LD is often much larger than the respective CD. When we aim to measure the CD of such particles, we should therefore take great care to avoid any leakage of the much stronger LD into the weak CD signal. In chapter 2 we used a single, square-modulation scheme of the polarization, performed by an EOM. We aimed to modulate between purely left and purely right circular polarization. In principle, a square wave modulation of the polarization is an ideal scheme to measure circular dichroism, as it completely avoids linear polarization states. However, this scheme requires a virtually perfect square-wave modulation of the polarization. This is practically not feasible when performing the modulation at high frequencies (>10 kHz), in particular due to bandwidth limitations of the electronics and piezoelectric behaviour of the EOM crystal. Any imperfection of the square-wave pattern can lead to a cross talk of LD and CD, thereby creating artefact signals. Secondly, the EOM, on top of the polarization modulation, also performs a slight modulation of the intensity. This effect is called residual amplitude modulation (RAM) [16] and it will induce an artefact signal for any absorbing particle.

To avoid both effects, the cross talk between LD and CD as well as the RAM, we exploited past developments in the field of CD spectroscopy [10, 22, 23], where two or more polarization modulators are used simultaneously to analyze different combinations of the driving frequencies of the two modulators, thereby giving access to various sample properties. We perform lock-in detection and thus only measure at a single frequency. But we still benefit of the two-modulator scheme if we perform our measurement at the sum (or

difference) frequency of the two modulators. We will describe in section 3.5.3 how to measure different absorptive properties at the sum frequency of the two modulators by using different static retarders placed after the modulators. At the sum frequency the modulators' individual residual amplitude modulation is of second order in these small effects, and can be neglected. In the following we will describe an alignment procedure that solves the problem of cross talk between LD and CD. Here we also benefit from the two-modulator scheme as it provides additional tuning parameters that allow us to remove cross talk better.

We concluded from the measurements in chapter 2, that a perfect square-wave modulation of the polarization by the EOM is not feasible and therefore we use a sinusoidal modulation of the polarization. Because of its mechanical resonance, the PEM only provides sinusoidal modulation. In both cases, the retardance created by each individual modulator varies sinusoidally with time and thereby not only creates circular but also elliptical and linear polarization states. One might think that this would inevitably cause cross talk between LD and CD. However, when we choose suitable modulation parameters and perform a thorough alignment of the components we can probe all absorptive properties of a sample with negligible cross talk between them. As illustrated in figure S3.1 the dual modulation of the polarization is performed using an EOM and a PEM. The laser beam first passes the EOM, then the PEM. We found that this arrangement order of the two modulators is convenient for the rejection of LD induced artefacts, because the static birefringence of the EOM can be more easily adjusted to compensate for imperfections of the polarization optics.

Alignment protocol

The alignment procedure we developed is composed of two steps. In the first step we align the fast axes of all components and make their optical axes collinear with the beam propagation. As the EOM contains a thick uniaxial crystal we must carefully align its crystal axis along the laser beam. In the first alignment step we make sure that the setup gives a CD response with the proper polarization optics. The second step is dedicated to ensure a pure CD measurement of the setup, free from cross talk. Later, we will also discuss how to probe other absorptive properties. The protocol that we developed is as follows:

First, we make sure that we have a well-defined and clean linear polarization state. To this purpose, we use a Glan-Thomson polarizer (extinction ratio 10^{-5}) oriented such that we have horizontally polarized light, or in terms of Stokes parameters: $S_1 = 1$. To measure the polarization state we use a Schaeffter & Kirchhoff polarization analyzer, which conveniently displays the polarization state in terms of the Stokes parameters. After the polarizer we send the laser beam through the EOM. For the rough alignment procedure the time-dependent retardation of both modulators is turned off.

EOM alignment: We first roughly align the EOM fast axis to 45° with respect to the initial polarization. Then we align the EOM's extraordinary axis along the propagation direction according to the alignment procedure described in [44]. Finally we align the EOM's fast axis precisely at 45° with respect to the initial polarization. Assuming that we have purely horizontal linearly polarized light $S_1 = 1$ and $S_2 = 0$, if the EOM's fast axis was aligned perfectly at 45° with respect to the initial polarization, when applying a retardation along the fast axis we would not create an S_2 component but only a S_3 component of the polarization. To align the fast axis we thus measure the polarization state while applying a large static retardation and rotate the EOM along its crystal axis, until the S_2 component vanishes.

PEM alignment: The alignment of the PEM is simpler, for it consists of fused silica instead

of a uniaxial crystal, thus there is no crystal axis the beam needs to be aligned to. However, the path length of the beam through the crystal defines the phase retardation and therefore we make sure we align the surface normal of the silica plate with the propagation axis of the laser beam. The retardation amplitude of the PEM is also slightly dependent on the position where the laser beam impinges on the quartz plate. To make sure that we exert the desired retardation amplitude we manually place the PEM such that we hit the center of the quartz plate. The PEM fast axis alignment is performed similar to the EOM fast axis alignment, but while applying a dynamic retardation instead.

Alignment of QWP: After the PEM, the laser beam passes through a number of static linear and circular birefringent components that allow us to set the operation mode of the setup. To be sensitive to CD, the differential absorption of left and right circularly polarized light, we need to insert a QWP after the two modulators. The achromatic QWP (Thorlabs) is mounted in a rotational optical mount to ensure precise alignment of the fast axis. To align it we measure the polarization state after the QWP while rotating the fast axis so that the polarization state is purely circular, $|\,S_3\,| = 1$.

Alignment of CB plates: The setup contains two circular birefringent components that can change the measurement mode in case we want to measure LD. Both of them are circularly birefringent plates, made from crystalline α-quartz, with a rotatory strength of either 45° or 90° (at $532\,\mathrm{nm}$). We will later come back to explain the purpose of these plates, for now we only explain their alignment. A purely circularly birefringent component does not possess a fast axis, but the path length of the laser beam through the component defines the rotatory strength of the plate. The path length can be adjusted by tilting the surface normal of the plate with respect to the propagation direction of the laser beam. We first measure the polarization state before we insert the plates. Assuming a perfect horizontal polarization, $S_1 = 1$, before the circular birefringent plates, we get $S_2 = -1$ for the CB_{45} plate and $S_1 = -1$ for the CB_{90} plate. The procedure that we discussed so far was the rough alignment procedure. If we chose suitable combinations of the static retarding elements we would already be able to measure different properties of an absorbing sample. However, these measurements might not be free from cross talk between LD and CD. A second step of alignment is required to make it exclusively sensitive to a single absorptive property, meaning that we suppress the cross talk between LD and CD. Up to now, the time-dependent retardation of the polarization modulators was turned off. For this second step, both modulators are set to perform a non-biased sinusoidal modulation with a retardation amplitude of $\pi/2$, the EOM at frequency ω_1 and the PEM at frequency ω_2. We insert a photodiode and a rotatable polarizer (calibration polarizer), as illustrated in figure S3.1. The polarizer represents a purely linear dichroic element. The photodiode is connected to a lock-in amplifier, which is referenced to the sum frequency of the two modulators. We bring the setup to the CD-sensitive mode, which corresponds to the configuration with two modulators plus the QWP. As we modulate the polarization with both modulators, the intensity transmitted through the calibration polarizer changes as a function of time. The lock-in compares the intensity transmitted through the polarizer with the external reference ($\omega_1 + \omega_2$) while extracting modulations occurring only at this very frequency. We shall thus call the part of the transmitted intensity that is modulated at frequency $\omega_1 + \omega_2$ our signal. If we are in CD-sensitive mode, no signal is expected when the calibration polarizer is inserted, as it is only linearly but not circularly dichroic. However, due to slight imperfections in the modulation scheme, such as misalign-

ment of the fast axes of the EOM, PEM or QWP, bias retardation of the modulators, or deviation of the QWP's retardation strength, we have to anticipate a nonzero cross talk of LD and CD and therefore also a signal. The strength of the signal measured by the lock-in, while the polarizer is inserted, is a measure of the cross talk between LD and CD. We found that we can compensate the aforementioned imperfections of the components and the alignment, thereby we reduce the cross talk. To achieve this it is sufficient to adjust two parameters, the EOM bias retardation and the QWP's fast axis.

Fine alignment procedure: First we rotate the calibration polarizer such that it transmits S_1 = 1 and we minimize the lock-in signal at the sum frequency by adjusting the EOM's bias retardation. Then we rotate the calibration polarizer to transmit S_2 = 1 and minimize the signal by adjusting the fast axis of the QWP. To understand this second alignment procedure it is important to have a closer look at LD. Linear dichroism which is defined as the differential absorption of two orthogonal polarization states is, unlike CD, dependent on the in-plane orientation of the object under study. To retrieve the full linear dichroic behaviour of an object, two measurements are necessary, one where we probe the absorption difference of S_1=1 and S_1=-1, which we shall call $LD_{\perp}$, and one where we probe the absorption difference of S_2 =1 and S_2=-1, and which we call $LD_{\swarrow}$. When we try to avoid cross talk of LD and CD we need to make sure to avoid cross talk of both $LD_{\perp}$ with CD and $LD_{\swarrow}$ with CD. We found that the change of the EOM bias retardation affects exclusively the cross talk between $LD_{\swarrow}$ and CD, while the rotation of the QWP's fast axis affects exclusively the cross talk between $LD_{\perp}$ and CD, at least within a reasonable range. This behaviour is represented in figure 3.2.

Quantification of the extinction ratio

With the calibration insert, shown in figure S3.1, which is composed of the rotatable polarizer and the photodiode, we can not only tune the setup for reducing the cross talk, but we are also able to quantify this cross talk. This is especially important when measuring particles that have strong LD compared to their CD, such as plasmonic nanorods, or plasmonically coupled metal nanospheres. [45–47]. Although we achieve very high rejection of cross talk we are not able to completely eliminate it. To quantify the residual cross talk we define a rejection ratio, that tells by which factor we suppress the leakage of LD into CD. The experimental extinction ratio is defined as:

$$R_{ext}(\alpha) = \frac{LD_{pol}}{CD_{pol}}. \tag{3.2}$$

To determine the rejection ratio we need to measure the two quantities CD_{pol} and LD_{pol}. Therefore we first put the setup in $LD_{\swarrow}$ -sensitive mode and rotate the calibration polarizer to maximize the lock-in signal. The obtained maximum value is LD_{pol}. Then we switch to CD-sensitive mode by inserting the QWP and again measure the lock-in signal. The obtained value is CD_{pol}. CD_{pol} is in general dependent on the angle of the polarizer. This indicates that there is a different amount of cross talk from $LD_{\swarrow}$ into CD, and from $LD_{\perp}$ into CD. We typically measure a rejection of 200 at polarizer positions of $n \cdot 90°$. For polarizer positions of $45° + n \cdot 90°$ we measure a rejection ratio of $6{\times}10^4$. For our measurements we assume the worst case corresponding to the lowest rejection ratio, 200. We want to note here that this rejection ratio is mutual. If we suppress the LD leakage into CD we also suppress the leakage of CD into LD.

In case we seek to have even stronger rejection of cross talk we make use of the aforementioned CB_{90} plate as described in [22]. The CB_{90} plate rotates all linear polarization states by 90° regardless of their orientation. This effectively flips the sign of LD, while maintaining its magnitude. On the other hand, as the CB_{90} plate does not affect circular polarization states, the circular dichroism measurement is not affected. Thus, in order to even further reduce the cross talk, we can perform two circular dichroism measurements, one with and one without the CB_{90} plate. If we then average these two measurements we remove the residual LD contribution.

3.5.3. Simulations

In a dual polarization modulation scheme, the time-dependent power absorbed by a sample can be composed of many different combinations of the frequencies driving the two modulators, ω_1 and ω_2, depending on the properties of the sample under study. In this section we want to simulate the time-dependent power absorbed by a given sample using Jones matrix calculus. We then extract the frequency spectrum by applying a FFT of the absorbed power. In principle one could also perform an analytical calculation of the frequency decomposition of an arbitrary sample as presented in [23]. However, our numerical approach allows us to conveniently explore a large space of parameters, which would be tedious to calculate with an analytical approach.

Jones matrix representation of the optical components
The matrix formalism developed by Jones [48–54] provides a convenient framework for analyzing the effects of optical components on fully polarized light. The matrix representations for the different optical components were taken from references [48, 51, 54].
Rotation Matrix:

$$\mathbf{R}_\Theta = \begin{bmatrix} cos(\Theta) & sin(\Theta) \\ -sin(\Theta) & cos(\Theta) \end{bmatrix}, \tag{3.3}$$

With the rotation matrix $\mathbf{R}_\Theta$ it is possible to calculate the matrix representation of axially rotated elements. Assuming that the optical component has a matrix representation of $\mathbf{M}$ in a certain reference frame, when the component is rotated by an angle Θ in clockwise sense, then the matrix of the rotated element can be expressed as $\mathbf{M}_\Theta = \mathbf{R}(-\Theta)M\mathbf{R}(\Theta)$.
Linearly birefringent plate:

$$\Phi(\eta, \Theta) = \mathbf{R}(-\Theta) \begin{bmatrix} 1 & 0 \\ 0 & e^{i\eta} \end{bmatrix} \mathbf{R}(\Theta). \tag{3.4}$$

In the simplest case of a static birefringent plate, η is a constant value. We can model a polarization modulator with a time-dependent retardance as $\eta(t) = \eta_0 sin(\omega t) + \phi_0$, where η_0 is the retardation amplitude, ω the modulation frequency and ϕ_0 an additional static linear birefringence.
Circularly birefringent plate:

$$\mathbf{CB}_\alpha = \begin{bmatrix} cos(\alpha) & sin(\alpha) \\ -sin(\alpha) & cos(\alpha) \end{bmatrix}, \tag{3.5}$$

with α being the rotatory strength (optical activity) of the CB plate. With the above defined Jones matrices and for horizontally polarized light as input, we can write the time-dependent electric field of the polarization modulator setup that is illustrated in figure S3.1 as

$$\begin{bmatrix} E_{x0} \\ E_{y0} \end{bmatrix}(t) = \mathbf{CB}_\alpha \, \Phi_0(\eta_0, \Theta_0) \, \Phi_2(\eta_2, \Theta_2, \omega_2, t) \, \Phi_1(\eta_1, \Theta_1, \omega_1, t) \begin{bmatrix} 1 \\ 0 \end{bmatrix}, \tag{3.6}$$

where $\Phi_{1,2}$ represent the matrices of the polarization modulators and Φ_0 a static linear retarder (QWP). Often, the Jones matrix approach is used to calculate the light transmitted

through a sample. This approach represents the CD measurements performed with commercial CD spectrometers well, as they measure the transmission of a dilute solution of molecules in a cuvette. The measurements that we perform, however, are true absorption measurements and therefore require a different matrix representation of the samples in terms of absorption. This representation has been described by Jones in [54]. The different absorptive properties of a sample can be modeled as follows:
Isotropic absorber:

$$\mathbf{u} = \kappa \begin{bmatrix} u & 0 \\ 0 & u \end{bmatrix}, \tag{3.7}$$

with κ being the amplitude absorption coefficient.
LD$_\perp$ absorber:

$$\mathbf{ld}_\perp = \mathbf{p}_\perp \begin{bmatrix} 1 & 0 \\ 0 & -1 \end{bmatrix}, \tag{3.8}$$

with $\mathrm{p}_\perp$ being half the difference of the two principal absorption coefficients.
LD$_\diagup$ absorber:

$$\mathbf{ld}_\diagup = \mathbf{p}_\diagup \begin{bmatrix} 0 & 1 \\ 1 & 0 \end{bmatrix}, \tag{3.9}$$

with $\mathrm{p}_\diagup$ being half the difference of the two principal absorption coefficients.
CD absorber:

$$\mathbf{cd} = \delta \begin{bmatrix} 0 & -i \\ i & 0 \end{bmatrix}, \tag{3.10}$$

with δ being half the difference of the absorption coefficients of left and right circular polarization. With the definitions for the samples given in equations 3.7-3.10 it is possible to represent an absorber exhibiting various absorptive properties by just adding the respective sample matrices. Assuming the particle under study behaves as a dipole, the time-averaged power absorbed by the particle can be expressed as

$$\langle \mathcal{P}_{abs} \rangle(\omega_1, \omega_2) = -\langle Im\big[\vec{p}^{*}(\omega_1, \omega_2) \cdot \vec{E}(\omega_1, \omega_2\big] \rangle \tag{3.11}$$

with

$$\vec{p} = \overset{\leftrightarrow}{\alpha} \vec{E} \tag{3.12}$$

where $\vec{p}$ is the dipole moment and $\overset{\leftrightarrow}{\alpha}$ the polarizability tensor of the absorbing dipole [55]. When we refer to the time average we imply time average over the optical frequencies, but not the frequencies of the polarization modulators, this is indicated by the (ω_1, ω_2) dependence. In general, when performing a transmission assay, one would measure the extinction and not the absorption, in which case one also would need to take the real part of the polarizability into account. In photothermal microscopy, as we perform a true absorption measurement, we must only take the imaginary part of the polarizability into account [56], which can be expressed by linear combinations of equations 3.7-3.10.

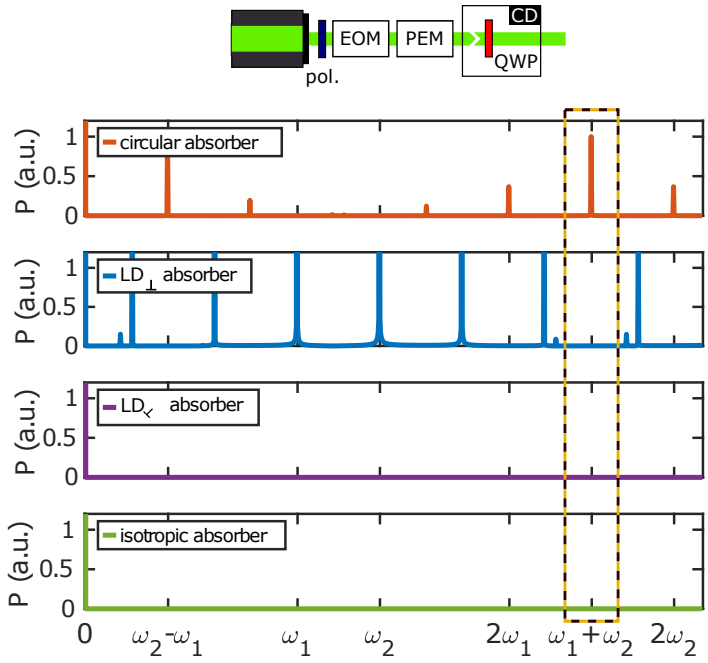

Figure S3.2: Spectrum of the absorbed power of the four different absorbers, exhibiting either only CD, $LD_{\perp}$, $LD_{\swarrow}$ or isotropic absorption, under dual polarization modulation in CD-sensitive mode. We normalize the power to 1 for the circular absorber at the sum frequency ω_1+ω_2.

Simulated FFT spectra of different absorbers

In our simulations we investigate the time-dependent absorbed power of samples exhibiting different absorptive properties. We first calculate the absorbed power, according to equation 3.11, for the four different absorptive properties defined in 3.7-3.10, and plot it in the frequency domain by applying a FFT. Figure S3.2 shows the frequency spectra of four absorbers exhibiting either pure CD, pure $LD_{\perp}$, pure $LD_{\swarrow}$ or pure isotropic absorption. The spectra are calculated for the CD - setup configuration. For the differential absorptivities we choose δ=10^{-3}, $p_{\perp}$ and $p_{\swarrow}$ =5×10^{-2} and κ=0.5. In CD mode, if we extract the signal at the sum frequency ω_1+ω_2, we only have a contribution from the circular dichroic sample. If we want to measure the other absorptive properties at the sum frequency we have to change the mode of the setup as discussed in section 3.5.2. In our computational model this is done by modifying the components of equation 3.6. Figure S3.3(a) shows the spectrum of the absorbed power of the same set of absorbers in $LD_{\perp}$ sensitive mode. We can indeed observe that the linear dichroic absorber $LD_{\perp}$ has a component at ω_1+ω_2. Likewise figure S3.3(b) shows the power spectrum of the same set of absorbers now in the $LD_{\swarrow}$ sensitive mode. As expected only the $LD_{\swarrow}$ absorber has a component at the sum frequency ω_1+ω_2. Note that in all three cases (figures S3.2 and 3.3), the isotropic absorber only shows constant absorption (at f = 0), which is also expected as we do not perform intensity but only polarization modulation. Until now we have only considered ideal conditions, in which we

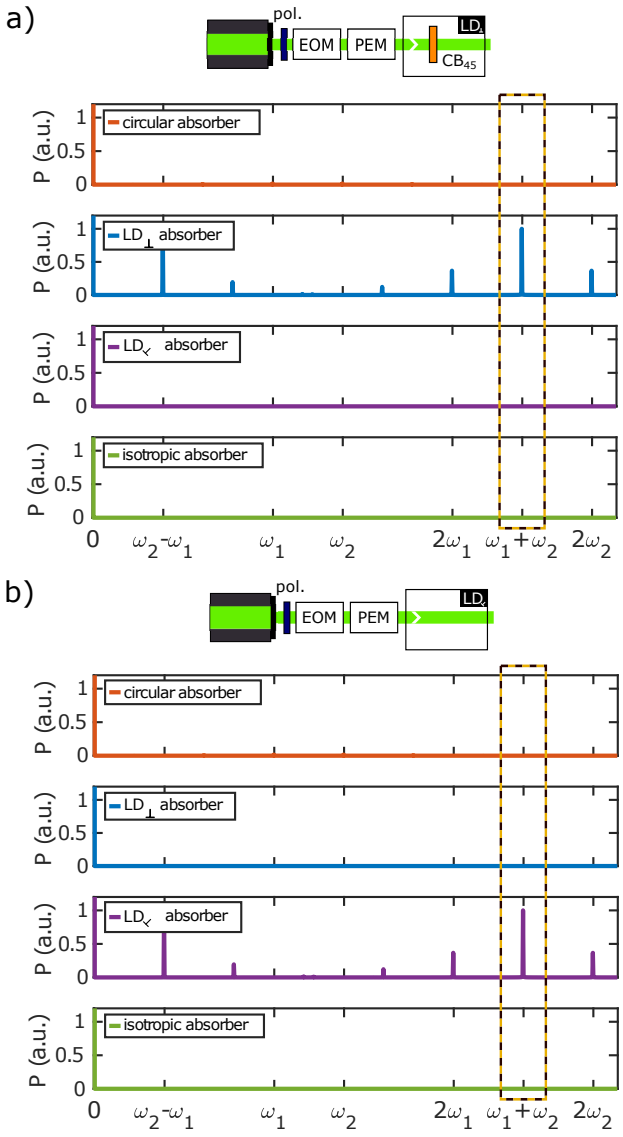

Figure S3.3: Spectrum of the absorbed power of the four different absorbers, exhibiting either CD, $LD_{\perp}$,$LD_{\swarrow}$ or isotropic absorption, under dual polarization modulation. In (a) for $LD_{\perp}$ sensitive and (b) $LD_{\swarrow}$ sensitive mode. We normalize the power to be 1 for (a) the $LD_{\perp}$ absorber and for (b) $LD_{\swarrow}$ the absorber, at the sum frequency $\omega_1+\omega_2$.

can easily ensure zero cross talk between LD and CD, and there is no artefact signal due to residual amplitude modulation. In a real setup we have to consider imperfections of the optical components themselves as well as slight misalignment of the various components.

Owing to our numerical approach we can easily simulate the effect of these imperfections. These imperfections will have an effect on the spectrum of the absorbed power and introduce a cross talk between the different absorptive properties. To illustrate the influence of one particular configuration we now introduce the following set of imperfections:

- EOM residual intensity modulation of 10^{-3}
- PEM residual intensity modulation of 10^{-3}
- PEM fast axis misalignment of 0.5°
- QWP deviation of $\pi/200$ from $\pi/2$ retardation

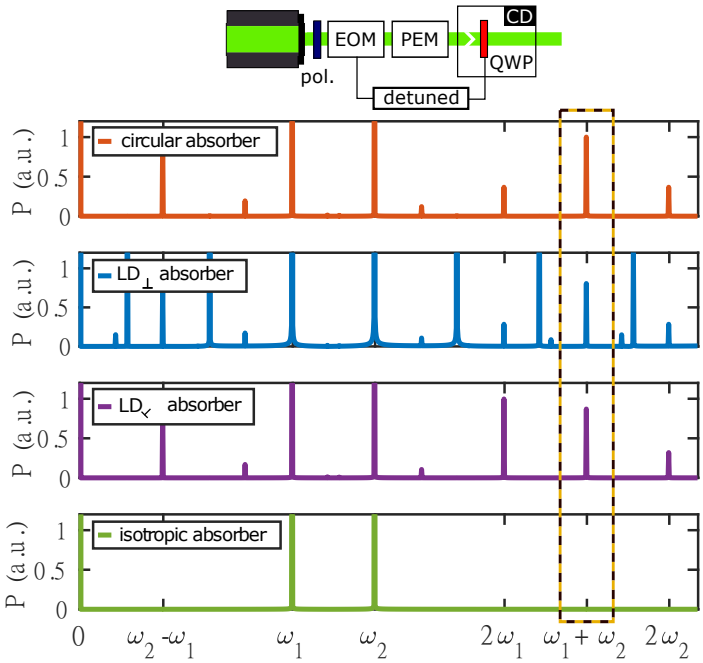

Figure S3.4: Spectrum of the absorbed power of the four different absorbers, under dual polarization modulation with additional imperfections of the modulation scheme, which lead to cross talk of linear and circular dichroism. We normalize the power to be 1 for the circular absorber at the sum frequency ω_1+ω_2.

In case the g-factor of CD and LD in a sample is of the same order of magnitude, small imperfections would not have a great impact on the CD measurement. However, when investigating the CD of plasmonic nanoparticles such as nanorods, the effect of LD can be much stronger. Therefore, in our simulations, we set the CD to be a factor of 50 weaker than the LD. Figure S3.4 shows the power spectrum in CD-sensitive mode under the aforementioned imperfections of the polarization modulation. In this case, also the $LD_{\perp}$ as well as the $LD_{\swarrow}$ show power absorption at the sum frequency, indicating a cross talk of LD into CD. As opposed to figures S3.2-S3.3 here the isotropic absorber shows a frequency

component at ω_1 and ω_2 which is due to the slight residual intensity modulation of the polarization modulators. The set of imperfections that we have used here is just one single example, other combinations are possible depending on the alignment and the individual components. In general there can also be more sources of imperfections induced by other optical components that we have not discussed so far for simplicity. These can be additional optical components in the beam path. We found that with the alignment protocol described in the above sections we can compensate also for small birefringent and dichroic effects on the polarization exhibited by these additional components.

3.5.4. CD of gold nanoparticle dimers

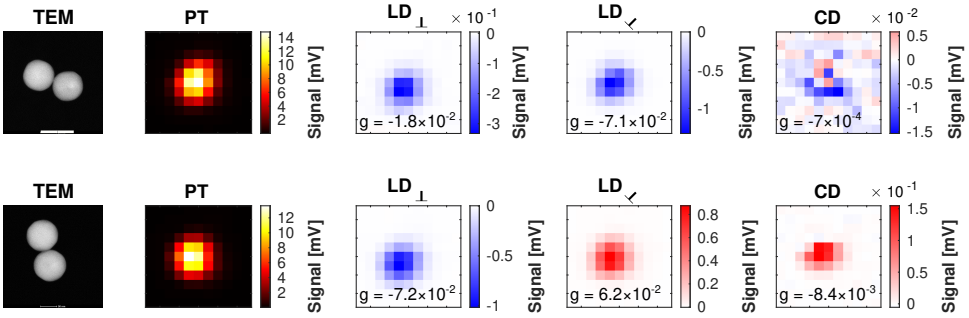

Figure S3.5: Correlated TEM images and optical measurements of two different 100 nm diameter gold nanoparticle dimers. One dimer is showing relatively strong PT CD signal, the other one shows weak CD signal. The measurements were performed at a heating wavelength of 532 nm. The scale bar in the TEM image is 100 nm.

Figure S3.5 shows correlated TEM and optical measurements of two dimer gold nanoparticles. The measurements are carried out in immersion oil as photothermal medium. One dimer exhibits relatively strong CD of 0.8%, the second particle exhibits a CD of 0.07% which is one magnitude lower. The $LD_{\perp}$ and $LD_{\swarrow}$ are both one or two orders of magnitude larger than the CD values, which probably is induced by plasmonic hybridization.

3.5.5. CD of a single gold nanoparticle in carvone with LD reference

Figure S3.6 shows absorption scans of a single gold nanoparticle. The particle was chosen such that it exhibits both weak CD and weak LD, to make sure that there is no residual leakage of LD into CD and that thermal induced reshaping does not decrease the CD over the course of the experiment shown in figure 3.5. The corresponding g-factors of LD and CD are indicated in the scans. If we take into account our previously shown LD rejection ratio of 300 we expect a residual leakage of LD into CD of not larger than 5×10^{-5} in g-factor which is one magnitude lower than the particles' actual CD g-factor.

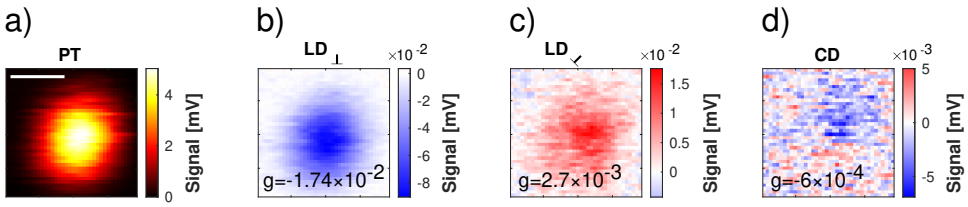

Figure S3.6: PT (a) $LD_{\perp}$ (b) $LD_{\swarrow}$ (c) and CD (d) scans of the single 100 nm diameter spherical gold nanoparticle in figure 3.5. All measurements here were carried out in R-carvone. The scale bar is 250 nm. The inserts of (b)-(d) show the respective g-factors.

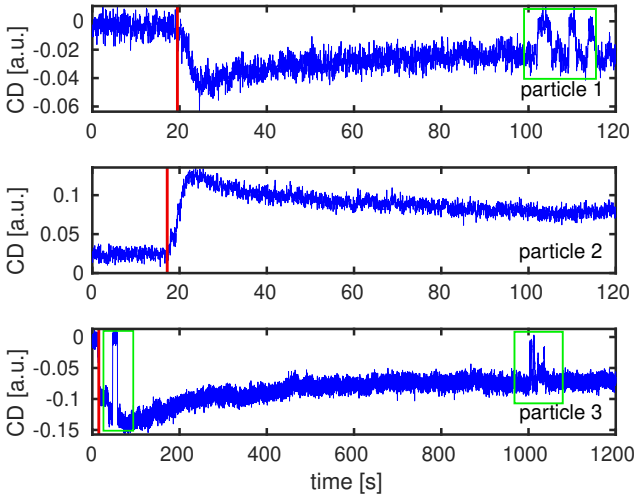

Figure S3.7: Time trace of CD measurements of three different 100 nm gold nanoparticles at high heating laser power indicating reshaping of the nanoparticles. At the beginning of each timetrace, the laser power is kept very low and after about 20 seconds, the laser power is slowly raised to the highest laser power. The highest laser power is about 30 mW, 30 mW and 40 mW for the first, second and third particle, respectively. The heating power (wavelength of 532 nm) is spread over an area of about 20 µm. We use 10 mW of probe power (laser wavelength of 815 nm) in confocal. The binning time is 30 ms. The red line indicates the time when we increase the heating laser power and green boxes indicate where we did manual refocusing to check that the decrease in signal is indeed due to the reshaping, but not due to any drift out of focus. The first green box in the timetrace for the third particle indicates when the heating laser was blocked for a short period of time.

3.5.6. Heat-induced reshaping

Figure S3.7 shows time traces of three different single gold nanoparticles. We first focus on a particle with a low laser power of few mW. After a given time, indicated by the red line in figure S3.7 we slowly increase the power of the heating beam by about 30 mW to 40 mW (Koehler illumination in the area of 20 μm^2). The green boxes indicate where we manually refocus to check that the decrease in signal is indeed due to the reshaping, but not due to the out-of-focus drifts. After the initial increase, which is due to the increase in heating power,

we observe a gradual decrease of CD signal, which is due to reshaping. Notably the CD signal does not vanish completely even after hundreds of seconds, but stabilizes at some finite value. This is probably because of the limited heating laser power in our experiments. We think that a further increase in heating laser power could induce further reshaping and lead to weaker and weaker CD signals over longer periods of laser exposure. However, the laser power cannot be increased indefinitely, as light-induced reactions were observed to take place in such complex liquids as carvone [40].

3.5.7. Nanofabrication of single aluminium nanorods

Aluminium nanostructures were fabricated in the Kavli Nanolab in Delft, using the following protocol in chronological order. Glass coverslips (borosilicate glass, diameter $25\,\mathrm{mm}$, thickness No.1) were used as substrate. First, they were cleaned by sonication in acetone and isopropanol. The substrate was dehydrated by a bake-off at $150\,^{\circ}\mathrm{C}$ for 10 minutes and in the same equipment it underwent priming with a monolayer of HMDS (Delta RC80 apparatus) to improve the hydrophobicity of the glass surface. The samples were transferred to a spin-coater and spun with CSAR positive e-beam resist (AR-P 6200.04) at $2000\,\mathrm{rpm}$ followed by a soft bake for $2\,\mathrm{min}$ on a hotplate at $150\,^{\circ}\mathrm{C}$. After that, the CSAR layer was covered with $11\,\mathrm{nm}$ of chromium through e-beam evaporation, to form a conducting layer on top of the samples and to prevent charging of the substrate during e-beam patterning. The samples were e-beam exposed with a pattern that contained arrays of aluminium rods. The dimensions of the rods were $40\times100\,\mathrm{nm}$. Each array was exposed at a different dose, ranging from 70 to $200\,\mu\mathrm{C/cm^2}$. Eventually the optimal dose was chosen by means of the optical experiment. Next, the samples were stripped of chromium by submerging them in a Cr01 TechniEtch solution for $15\,\mathrm{s}$ and rinsing them with DI water. The samples were first developed in pentyl acetate ($1\,\mathrm{min}$), then a mixture of isopropanol and methyl-isobutyl ketone (1:1) for $1\,\mathrm{min}$ and finally in isopropanol for $1\,\mathrm{min}$. The samples were dried and subsequently residues of the developed resist were removed through a descum process by oxygen plasma etching for $30\,\mathrm{s}$ at 100 Watt power and $200\,\mathrm{sccm}$ O_2 flow. The exposed, developed and oxygen etched glass samples were then e-beam evaporated with $3\,\mathrm{nm}$ of Cr for adhesion, directly followed by $60\,\mathrm{nm}$ of aluminium. Lift-off was performed in anisole at $80\,^{\circ}\mathrm{C}$ for at least 1 hour. Finally, the samples were rinsed of all residuals in a jet of acetone followed by rinsing in a beaker with isopropanol and drying in a N_2 stream.

References

[1] Lombardi, R. A.; Nafie, L. A. Observation and Calculation of Vibrational Circular Birefringence: A New Form of Vibrational Optical Activity. *Chirality* **2009**, *21*, E277–E286.

[2] Hendry, E.; Mikhaylovskiy, R.; Barron, L.; Kadodwala, M.; Davis, T. Chiral Electromagnetic Fields Generated by Arrays of Nanoslits. *Nano Letters* **2012**, *12*, 3640–3644.

[3] Tang, Y.; Cohen, A. E. Enhanced Enantioselectivity in Excitation of Chiral Molecules by Superchiral Light. *Science* **2011**, *332*, 333–336.

[4] Schaeferling, M.; Dregely, D.; Hentschel, M.; Giessen, H. Tailoring Enhanced Optical

Chirality: Design Principles for Chiral Plasmonic Nanostructures. *Physical Review X* **2012**, *2*, 031010.

[5] Zhang, Q.; Hernandez, T.; Smith, K. W.; Hosseini Jebeli, S. A.; Dai, A. X.; Warning, L.; Baiyasi, R.; McCarthy, L. A.; Guo, H.; Chen, D.-H.; Dionne, J. A.; Landes, C. F.; Link, S. Unraveling the Origin of Chirality from Plasmonic Nanoparticle-Protein Complexes. *Science* **2019**, *365*, 1475–1478.

[6] Raziman, T.; Godiksen, R. H.; Muller, M. A.; Curto, A. G. Conditions for Enhancing Chiral Nanophotonics near Achiral Nanoparticles. *ACS Photonics* **2019**, *6*, 2583–2589.

[7] Solomon, M. L.; Abendroth, J. M.; Poulikakos, L. V.; Hu, J.; Dionne, J. A. Fluorescence-Detected Circular Dichroism of a Chiral Molecular Monolayer with Dielectric Metasurfaces. *Journal of the American Chemical Society* **2020**, *142*, 18304–18309.

[8] Maoz, B. M.; Chaikin, Y.; Tesler, A. B.; Bar Elli, O.; Fan, Z.; Govorov, A. O.; Markovich, G. Amplification of Chiroptical Activity of Chiral Biomolecules by Surface Plasmons. *Nano Letters* **2013**, *13*, 1203–1209.

[9] García-Guirado, J.; Svedendahl, M.; Puigdollers, J.; Quidant, R. Enantiomer-Selective Molecular Sensing Using Racemic Nanoplasmonic Arrays. *Nano Letters* **2018**, *18*, 6279–6285.

[10] Jellison, G.; Modine, F. Two-Modulator Generalized Ellipsometry: Theory. *Applied Optics* **1997**, *36*, 8190–8198.

[11] Jellison, G.; Modine, F. Two-Modulator Generalized Ellipsometry: Experiment and Calibration. *Applied Optics* **1997**, *36*, 8184–8189.

[12] Vinegrad, E.; Vestler, D.; Ben-Moshe, A.; Barnea, A. R.; Markovich, G.; Cheshnovsky, O. Circular Dichroism of Single Particles. *ACS Photonics* **2018**, *5*, 2151–2159.

[13] Novotny, L.; Hecht, B. *Principles of Nano-Optics*; Cambridge University Press: Cambridge, 2012.

[14] Bauer, T. Probe-Based Nano-Interferometric Reconstruction of Tightly Focused Vectorial Light Fields. **2017**,

[15] Spaeth, P.; Adhikari, S.; Le, L.; Jollans, T.; Pud, S.; Albrecht, W.; Bauer, T.; Caldarola, M.; Kuipers, L.; Orrit, M. Circular Dichroism Measurement of Single Metal Nanoparticles Using Photothermal Imaging. *Nano Letters* **2019**, *19*, 8934–8940.

[16] Whittaker, E. A.; Gehrtz, M.; Bjorklund, G. C. Residual Amplitude Modulation in Laser Electro-Optic Phase Modulation. *JOSA B* **1985**, *2*, 1320–1326.

[17] Sathian, J.; Jaatinen, E. Intensity Dependent Residual Amplitude Modulation in Electro-Optic Phase Modulators. *Applied Optics* **2012**, *51*, 3684–3691.

[18] Shindo, Y.; Nakagawa, M. Circular Dichroism Measurements. I. Calibration of a Circular Dichroism Spectrometer. *Review of Scientific Instruments* **1985**, *56*, 32–39.

[19] Shindo, Y.; Nakagawa, M.; Ohmi, Y. On the Problems of CD Spectropolarimeters. II: Artifacts in CD Spectrometers. *Applied Spectroscopy* **1985**, *39*, 860–868.

[20] Shindo, Y. On the Problems of CD Spectropolarimeter (IV) Artifacts Due to the Light Scattering by Small Particles. *Applied Spectroscopy* **1985**, *39*, 713–715.

[21] Cheng, J.; Nafie, L.; Stephens, P. Polarization Scrambling Using a Photoelastic Modulator: Application to Circular Dichroism Measurement. *JOSA* **1975**, *65*, 1031–1035.

[22] Barriel, O. A. Mueller Matrix Polarimetry of Anisotropic Chiral Media. Ph.D. thesis, Universitat de Barcelona, Barcelona, 2010.

[23] Arteaga, O.; Freudenthal, J.; Wang, B.; Kahr, B. Mueller Matrix Polarimetry with Four Photoelastic Modulators: Theory and Calibration. *Applied Optics* **2012**, *51*, 6805–6817.

[24] Knight, M. W.; Liu, L.; Wang, Y.; Brown, L.; Mukherjee, S.; King, N. S.; Everitt, H. O.; Nordlander, P.; Halas, N. J. Aluminum Plasmonic Nanoantennas. *Nano Letters* **2012**, *12*, 6000–6004.

[25] Cheng, F.; Su, P.-H.; Choi, J.; Gwo, S.; Li, X.; Shih, C.-K. Epitaxial Growth of Atomically Smooth Aluminum on Silicon and Its Intrinsic Optical Properties. *ACS Nano* **2016**, *10*, 9852–9860.

[26] Jain, P. K.; El-Sayed, M. A. Plasmonic Coupling in Noble Metal Nanostructures. *Chemical Physics Letters* **2010**, *487*, 153–164.

[27] Shen, X.; Song, C.; Wang, J.; Shi, D.; Wang, Z.; Liu, N.; Ding, B. Rolling up Gold Nanoparticle-Dressed DNA Origami into Three-Dimensional Plasmonic Chiral Nanostructures. *Journal of the American Chemical Society* **2012**, *134*, 146–149.

[28] Kuzyk, A.; Schreiber, R.; Fan, Z.; Pardatscher, G.; Roller, E.-M.; Högele, A.; Simmel, F. C.; Govorov, A. O.; Liedl, T. DNA-Based Self-Assembly of Chiral Plasmonic Nanostructures with Tailored Optical Response. *Nature* **2012**, *483*, 311–314.

[29] Berciaud, S.; Lasne, D.; Blab, G. A.; Cognet, L.; Lounis, B. Photothermal Heterodyne Imaging of Individual Metallic Nanoparticles: Theory *versus* Experiment. *Physical Review B* **2006**, *73*, 045424.

[30] Selmke, M.; Braun, M.; Cichos, F. Photothermal Single-Particle Microscopy: Detection of a Nanolens. *ACS Nano* **2012**, *6*, 2741–2749.

[31] Narushima, T.; Okamoto, H. Circular Dichroism Microscopy Free from Commingling Linear Dichroism *via* Discretely Modulated Circular Polarization. *Scientific Reports* **2016**, *6*, 1–10.

[32] Govorov, A. O.; Fan, Z.; Hernandez, P.; Slocik, J. M.; Naik, R. R. Theory of Circular Dichroism of Nanomaterials Comprising Chiral Molecules and Nanocrystals: Plasmon Enhancement, Dipole Interactions, and Dielectric Effects. *Nano Letters* **2010**, *10*, 1374–1382.

[33] Govorov, A. O.; Fan, Z. Theory of Chiral Plasmonic Nanostructures Comprising Metal Nanocrystals and Chiral Molecular Media. *ChemPhysChem* **2012**, *13*, 2551–2560.

[34] Yoo, S.; Park, Q.-H. Enhancement of Chiroptical Signals by Circular Differential Mie Scattering of Nanoparticles. *Scientific Reports* **2015**, *5*, 1–8.

[35] Albrecht, W.; Deng, T.-S.; Goris, B.; van Huis, M. A.; Bals, S.; van Blaaderen, A. Single Particle Deformation and Analysis of Silica-Coated Gold Nanorods before and after Femtosecond Laser Pulse Excitation. *Nano Letters* **2016**, *16*, 1818–1825.

[36] Ruijgrok, P.; Verhart, N.; Zijlstra, P.; Tchebotareva, A.; Orrit, M. Brownian Fluctuations and Heating of an Optically Aligned Gold Nanorod. *Physical Review Letters* **2011**, *107*, 037401.

[37] Taylor, A. B.; Siddiquee, A. M.; Chon, J. W. Below Melting Point Photothermal Reshaping of Single Gold Nanorods Driven by Surface Diffusion. *ACS Nano* **2014**, *8*, 12071–12079.

[38] Lambert, J.; Compton, R.; Crawford, T. D. The Optical Activity of Carvone: A Theoretical and Experimental Investigation. *The Journal of Chemical Physics* **2012**, *136*, 114512.

[39] Reinscheid, F.; Reinscheid, U. Stereochemical Analysis of (+)-Limonene Using Theoretical and Experimental NMR and Chiroptical Data. *Journal of Molecular Structure* **2016**, *1106*, 141–153.

[40] Gaiduk, A.; Ruijgrok, P. V.; Yorulmaz, M.; Orrit, M. Making Gold Nanoparticles Fluorescent for Simultaneous Absorption and Fluorescence Detection on the Single Particle Level. *Physical Chemistry Chemical Physics* **2011**, *13*, 149–153.

[41] Li, M.; Razumtcev, A.; Yang, R.; Liu, Y.; Rong, J.; Geiger, A. C.; Blanchard, R.; Pfluegl, C.; Taylor, L. S.; Simpson, G. J. Fluorescence-Detected Mid-Infrared Photothermal Microscopy. *Journal of the American Chemical Society* **2021**, *143*, 10809–10815.

[42] Zhang, Y.; Zong, H.; Zong, C.; Tan, Y.; Zhang, M.; Zhan, Y.; Cheng, J.-X. Fluorescence-Detected Mid-Infrared Photothermal Microscopy. *Journal of the American Chemical Society* **2021**, *143*, 11490–11499.

[43] Ding, T. X.; Hou, L.; Meer, H. v. d.; Alivisatos, A. P.; Orrit, M. Hundreds-Fold Sensitivity Enhancement of Photothermal Microscopy in Near-Critical Xenon. *The Journal of Physical Chemistry Letters* **2016**, *7*, 2524–2529.

[44] Gooch & Housego, Pockels Cell Alignment in a Q-Switched Laser. 2017; `https://gandh.com/wp-content/uploads/2017/10/GH-PM-EO-Pockels-cell-alignment-for-single-pass-systems.pdf` accessed 17 March 2021.

[45] Besteiro, L. V.; Zhang, H.; Plain, J.; Markovich, G.; Wang, Z.; Govorov, A. O. Aluminum Nanoparticles with Hot Spots for Plasmon-Induced Circular Dichroism of Chiral Molecules in the UV Spectral Interval. *Advanced Optical Materials* **2017**, *5*, 1700069.

[46] Govorov, A. O. Plasmon-Induced Circular Dichroism of a Chiral Molecule in the Vicinity of Metal Nanocrystals. Application to Various Geometries. *The Journal of Physical Chemistry C* **2011**, *115*, 7914–7923.

[47] Nesterov, M. L.; Yin, X.; Schaferling, M.; Giessen, H.; Weiss, T. The Role of Plasmon-Generated Near Fields for Enhanced Circular Dichroism Spectroscopy. *ACS Photonics* **2016**, *3*, 578–583.

[48] Jones, R. C. A New Calculus for the Treatment of Optical Systems. I. Description and Discussion of the Calculus. *JOSA* **1941**, *31*, 488–493.

[49] Hurwitz, H.; Jones, R. C. A New Calculus for the Treatment of Optical Systems. II. Proof of Three General Equivalence Theorems. *JOSA* **1941**, *31*, 493–499.

[50] Jones, R. C. A New Calculus for the Treatment of Optical Systems. III. The Sohncke Theory of Optical Activity. *JOSA* **1941**, *31*, 500–503.

[51] Jones, R. C. A New Calculus for the Treatment of Optical Systems. IV. *JOSA* **1942**, *32*, 486–493.

[52] Jones, R. C. A New Calculus for the Treatment of Optical System.V. A More General Formulation, and Description of Another Calculus. *JOSA* **1947**, *37*, 107–110.

[53] Jones, R. C. A New Calculus for the Treatment of Optical Systems. VI. Experimental Determination of the Matrix. *JOSA* **1947**, *37*, 110–112.

[54] Jones, R. C. A New Calculus for the Treatment of Optical Systems. VII. Properties of the N-Matrices. *JOSA* **1948**, *38*, 671–685.

[55] Jackson, J. D. *Classical Electrodynamics*; Wiley: New York, 1999.

[56] Hugonin, J.-P.; Besbes, M.; Ben-Abdallah, P. Fundamental Limits for Light Absorption and Scattering Induced by Cooperative Electromagnetic Interactions. *Physical Review B* **2015**, *91*, 180202.